Ceramics International 52 (2026) 34457–34464

Contents lists available at ScienceDirect

Ceramics International

journal homepage: www.elsevier.com/locate/ceramint

Thermal and mechanical properties of double perovskite-type Ba_2YNbO_6 ceramic

S.F. Solodovnikov [a], M. Zeraati [b,*], A.B. Kuznetsov [a,c], E.S. Zolotova [a], A.R. Nasyrbaev [d], I.P. Gulyaev [a,e], I.K. Igumenov [a], R.A. Shutilov [a,**], E.A. Maksimovsky [a], D.P. Pishchur [a], V.N. Yudin [a], V.V. Lukashov [a,f], I.V. Korolkov [a], A.P. Maltsev [a,b], A.R. Oganov [b,***]

[a] Nikolaev Institute of Inorganic Chemistry SB RAS, Acad. Lavrentyev Ave. 3, Novosibirsk, 630090, Russia
[b] Skolkovo Institute of Science and Technology, Bolshoy Boulevard 30, bld. 1, Moscow, 121205, Russia
[c] Sobolev Institute of Geology and Mineralogy SB RAS, Acad. Koptyug Ave. 3, Novosibirsk, 630090, Russia
[d] National Research Tomsk Polytechnic University, Usova Str. 7, Tomsk, 634034, Russia
[e] Khristianovich Institute of Theoretical and Applied Mechanics SB RAS, Institutskaya Str. 4/1, Novosibirsk, 630090, Russia
[f] Kutateladze Institute of Thermophysics SB RAS, Acad. Lavrentyev Ave. 1, Novosibirsk, 630090, Russia

ARTICLE INFO

Keywords:
Double perovskite
Thermal barrier coatings
Molecular dynamics simulations
Thermophysical and mechanical properties

ABSTRACT

Using a combination of advanced theoretical calculations with experimental measurements, the phase stability, thermal and mechanical properties of double perovskite Ba_2YNbO_6 (BYNO) were investigated to evaluate its potential as a top coat material for thermal barrier coatings (TBCs). Theoretical calculations using large-scale molecular dynamics simulations with machine learning interatomic potentials, revealed that BYNO possesses a promising combination of low thermal conductivity and thermal expansion coefficient (TEC). Experimentally, BYNO powder was prepared by stepwise solid-state reactions at 1100−1500 °C, followed by spark plasma sintering (SPS) at 1700 °C. The measured elastic moduli, Vickers nanohardness, linear TEC, and thermal conductivity are in good agreement with our calculations. Both molecular dynamics (MD) simulations and differential scanning calorimetry (DSC) confirmed a tetragonal to cubic phase transition $Fm\bar{3}m \rightarrow I4/m$ in BYNO near −10 °C. However, the measured low-temperature dependence of the lattice parameter and TEC of BYNO showed no deviations that could be caused by minor changes in the structure and unit cell volume during the transition. At 1000°C, BYNO exhibits an experimental thermal conductivity of ~1.9 W/(m·K) and a linear TEC of ~9.6×10^{-6} K^{-1}, which are slightly lower than those of commonly used yttria-stabilized zirconia (YSZ). Combined with its satisfactory mechanical properties—a Young's modulus of 217 ± 15 GPa and a Vickers hardness of 7.18 ± 0.96 GPa—these characteristics suggest that BYNO may be a potential candidate material for TBC applications.

1. Introduction

Thermal barrier coatings (TBCs) are widely used to protect the hot-section metal components in aircraft engines and gas turbines, improving their operating efficiency. A typical TBC system consists of an oxidation-resistant bond coat alloy and a thermally insulating, corrosion-resistant ceramic top coat. The current standard material for the top coat is yttria-stabilized zirconia (YSZ), which is ZrO_2 doped with 6–8 wt% Y_2O_3. YSZ exhibits a relatively low thermal conductivity (~2 W/(m·K) at 1000 °C) and a sufficiently high linear thermal expansion coefficient (TEC) (11×10^{-6} K^{-1}) [1,2]. The major drawbacks of YSZ are its phase instability above 1200 °C, sintering, and high oxygen diffusion, which limit the operating temperatures and number of thermal cycles [3,4]. Therefore, there is a need to search for more advanced TBC materials with high thermal, phase, chemical and mechanical stability, low thermal conductivity, moderate TEC matching that of turbine blade alloy, and low oxygen diffusion at operating temperatures [1–4]. In the last two decades, many refractory oxides such as fluorites (Ce, *RE*)O_{2-x}, HfO_2–Y_2O_3, pyrochlores $RE_2Zr_2O_7$, garnets $RE_3Al_5O_{12}$, $Y_3Al_xFe_{5-x}O_{12}$, monazite-type $REPO_4$, magnetoplumbites $CaAl_{12}O_{19}$, $LaMgAl_{11}O_{19}$,

* Corresponding author.
** Corresponding author.
*** Corresponding author.
E-mail addresses: Majid.Zeraati@skoltech.ru (M. Zeraati), shutilovra@gmail.com (R.A. Shutilov), A.Oganov@skoltech.ru (A.R. Oganov).

https://doi.org/10.1016/j.ceramint.2026.02.315
Received 30 August 2025; Received in revised form 9 February 2026; Accepted 21 February 2026
Available online 22 February 2026

fergusonite-type $RETaO_4$, $RENbO_4$, etc. have been studied as potential successors to YSZ for TBC applications [1–5].

Perovskites ABO_3 have also been considered among the most promising oxides for TBC applications due to their high melting points, low Young's moduli, low sintering rates [2] and rich opportunities for modifying their structure, composition and properties through isomorphic substitutions at the *A* and/or *B* sites. Early investigations of perovskites as TBC candidates focused on materials such as $SrZrO_3$, $SrZrO_3$:Ln^{3+} (Ln = Yb, Gd), $BaZrO_3$ and $Ba(Mg_{1/3}Ta_{2/3})O_3$ [6,7]. Other studied perovskite-like oxides for TBCs were $CaZrO_3$, $La(Al_{1/4}Mg_{1/2}Ta_{1/4})O_3$, $BaLa_2Ti_3O_{10}$, $LnAlO_3$ (Ln = Y, Yb), $Ln_2SrAl_2O_7$ (Ln = La, Nd, Sm, Eu, Gd, Dy [1,2,4,5], $SrHfO_3$:Ln^{3+} (Ln = Y, Yb) [8], $SrCeO_3$ [9], $Ba(Sr_{1/3}Ta_{2/3})O_3$ [10], $LnTa_3O_9$ (Ln = La, Nd, Gd, Yb) [11]. However, the most promising perovskites turned out to have such drawbacks as displacive phase transitions ($SrZrO_3$), relatively high thermal conductivity and low TEC ($BaZrO_3$), low fracture toughness ($Ba(Mg_{1/3}Ta_{2/3})O_3$), as well as ionic conductivity of oxygen-deficient materials, poor chemical compatibility with thermally grown oxides and the formation of secondary phases for complex perovskites like $Ba(Mg_{1/3}Ta_{2/3})O_3$ and $La(Al_{1/4}Mg_{1/2}Ta_{1/4})O_3$ [10,12].

Double perovskites $A_2B'B''O_6$ represent potential alternatives to simple (ABO_3) and layered perovskites ($Ba(Mg_{1/3}Ta_{2/3})O_3$, $Ln_2SrAl_2O_7$, $BaLa_2Ti_3O_{10}$, etc.) as materials for TBCs. Most double perovskites have the rock-salt type cation ordering with the 2 × 2 × 2 superstructure relative to a simple perovskite [13]. The flexibility of double perovskites, with a wide variety of combinations of different cations in the *A*, *B*′, and *B*″ sites, determinate their attractive semiconducting, metallic, dielectric, magnetic, luminescent, ferroelectric, thermoelectric, and other properties.

Our attention was drawn to one of the representatives of this huge family of compounds, the thermally stable double perovskite Ba_2YNbO_6 (BYNO), which was proposed as a host for phosphors doped with Mn^{4+} or Ln^{3+} [14,15], and as a substrate material for the epitaxial growth of high-quality $YBa_2Cu_3O_7$ superconducting films [16–18]. The electrical properties of BYNO ceramics were studied in Refs. [16,19] but there is no available data on the application of BYNO as a top coat material for TBCs, and data on its basic thermophysical and mechanical properties are also lacking.

This study addresses this critical gap in knowledge by providing a proper exploration of the thermophysical and mechanical properties of BYNO relevant to TBC application. To evaluate BYNO potential as a next-generation TBC material, we used a combination of advanced theoretical calculations with experimental measurements. For theoretical predictions of BYNO properties, we calculated its thermal conductivity and TEC as a function of temperature and showed that they are suitable for TBCs. We then prepared BYNO ceramics and single crystals and investigated the crystal structure, TEC, thermal conductivity, $^{Young's}$ modulus, and nanohardness of BYNO ceramic. The results of this study support a positive assessment of BYNO as a promising TBC material.

2. Materials and methods

2.1. Computational methodology

To calculate thermal conductivity of BYNO, we employed two theoretical approaches. The first was the homogeneous non-equilibrium molecular dynamics (HNEMD) method [20,21], implemented in the GPUMD package [22,23]. The second approach involved solving the Boltzmann transport equation (BTE) [24–27] using an effective harmonic model (EHM) [28,29], as implemented in the Hipive [30] and ShengBTE [31] packages.

In the HNEMD method, a slightly non-equilibrium state is created by adding a small external driving force $\boldsymbol{F}_e$ for the atoms in the simulation box [32]. This driving force induces a non-equilibrium heat current $\langle \boldsymbol{J} \rangle_{ne}$, which is linearly related to F_e:

$$\frac{\langle J^{\mu}(t)\rangle_{\mathrm{ne}}}{TV} = \sum_{\nu} \kappa^{\mu\nu}(t) F_e^{\nu}, \tag{1}$$

where, $\kappa^{\mu\nu}$ is the thermal conductivity tensor, *T* is temperature, and *V* is volume of the system. To maintain temperature control, we used the Nose-Hoover chain (NHC) thermostat [24,33]. Due to large fluctuations of thermal conductivity during molecular dynamics simulations we used the cumulative average thermal conductivity as function of simulation time $\kappa(t)$:

$$\kappa(t) = \frac{1}{t}\int_0^t \frac{\langle J^{\mu}(s)\rangle_{\mathrm{ne}}}{TVF_e^{\nu}} ds \tag{2}$$

Finally, we applied quantum corrections to thermal conductivity at all temperatures.

TECs were calculated from T = −263 °C up to 1827 °C (10–2100 K) using classical molecular dynamics (MD) and path-integral MD (PIMD) [34–37]. Due to nuclear quantum effects (NQEs) occurring below the Debye temperature, it is essential to use PIMD. Above the Debye temperature, however, MD simulations are sufficiently accurate for predicting lattice parameters and TEC at high temperatures [38,39].

To calculate elastic properties, we employed the Voigt-Reuss-Hill [40–42] averaging scheme and machine learning potential (MTP) [43] to obtain the effective elastic moduli. To calculate the Vickers hardness, we used Chen's model $\left(HV = 2^{*}\left(\frac{G^3}{B^2}\right)^{0.585} - 3\right)$ [44].

Details for theoretical approaches, including potential validation, simulation parameters, and convergence tests, are provided in Appendix A.

2.2. Sample preparation and characterization

Commercial $BaCO_3$, Y_2O_3 and Nb_2O_5 (Reachem Co., Russia, purity >99.9%) were used as starting materials. The powders were ground in a ball mill and pre-calcined at 800 °C for 3 h to remove residual moisture. BYNO powder was prepared by annealing the mixture of $4BaCO_3 + Y_2O_3 + Nb_2O_5$ at 1100 °C for 4 h, 1300 °C for 4 h, 1500 °C for 4 h with two intermittent regrindings. The sintered BYNO powder was then fractionated and the 20–60 μm fraction was placed into a 12.7 mm diameter graphite die and underwent spark plasma sintering (SPS) using an SPS10-4 system (GT Advanced Technologies, USA). The SPS process was performed at 1700 °C for 10 min in a vacuum (1 Pa) under a pressure of 60 MPa, soaking time was 10 min, a heating rate of 100 °C/min and natural cooling. The bulk material was polished with a grinding and polishing machine Forcipol 1V (Metkon, Turkey). The density of the bulk BYNO samples (ρ) was measured by the Archimede's method in distilled water.

Small BYNO crystals for structure determination were grown in a Pt crucible by spontaneous crystallization from the molten mixture of $BaCO_3$, Y_2O_3, Nb_2O_5 and B_2O_3, which was soaked at 1450 °C for 3 h and then cooled at a rate of 6 °C/h to 1000 °C, followed by switching off the furnace.

Powder X-ray diffraction (PXRD) of the sintered BYNO powder and grown crystals was performed on a Tongda TD3700 diffractometer (CuKα radiation, the 2θ range of 5−70°) at room temperature. The crystal structure of BYNO was refined by the Rietveld method [45] using the GSAS-II program [46]; and the results are given in Table S1. The thermal behavior of BYNO was studied by low- and high-temperature powder X-ray diffraction in a vacuum in the range of −196 to 1300 °C using a Tongda TD3700 diffractometer with a thermal chamber (CuKα radiation, 2θ range of 15° to 70° with a step of 0.0191°, cooling and heating rates of 100 °C/min, isothermal holding for 10 min at each temperature). An external Si standard was used to control the 2θ correction. The unit-cell parameters were refined by the Le Bail method

[47] with the GSAS-II program [46]. The temperature dependence of the unit cell parameters of BYNO was approximated by a quadratic polynomial.

Single-crystal XRD data for structure determination were collected at room temperature with a Bruker D8 Venture diffractometer (MoKα radiation, ω- and φ-scans with 0.5° wide frames, Photon III 14 CPAD detector). Data reduction was performed using the APEX 3 suite [48]. The crystal structure was solved with ShelXT [49] and refined by the full-matrix least-squares method on F^2 with anisotropic atomic displacement parameters using the ShelXL [50] programs, assisted by the Olex2 GUI [51]. The details of the data collection and refinement are listed in Table S1.

High-temperature thermal analysis of a small BYNO sample was performed using a specially designed high-temperature microscope [52]. The sample was heated in a helium atmosphere using a tungsten coil at a rate of 100 °C/min to 2000 °C, and the temperature was controlled with a W-Re thermocouple and a photodiode.

Raman spectra of BYNO ceramics from regions with a cross-section of around 1 μm were recorded on a LabRAM Horiba single-stage spectrometer with a CCD Symphony (Jobin Yvon) detector with 2048 horizontal pixels. The laser power (514 nm line of an Ar^+ laser) at the sample was typically less than 0.1 mW. The spectral resolution was 3.0 cm^{-1}. The micromorphology of the samples was studied by scanning electron microscopy (SEM) using Jeol JSM 6700F (Japan) and Hitachi TM 3000 (Japan) devices.

The Vickers nanohardness and Young's modulus of the bulk BYNO were measured with a Nanoscan-4D + tester (Nauchspetspribor, Russia). One hundred indentations were made with the indenter at a load of 250 mN on a rectangular 10 × 10 grid with a step of 50 μm. The Oliver-Pharr method [53] was used for processing the experimental data.

A sample of ∅ 12.230 × 1.235 mm was used to measure the thermal diffusivity (α) on a DLF-1200 laser flash analyzer (TA Instruments, USA) at 303−1073 K in a high-purity nitrogen atmosphere. To reduce energy losses due to the reflection of laser radiation, the sample was coated with a thin layer of graphite (GRAPHITE 200 spray, Cramolin, Germany). Specific heat capacity (C_p) was measured in the range of −143 to 547 °C on NETZSCH 204 F1 Phoenix differential scanning calorimeter using an 80.36 mg BYNO sample and a 37.60 mg synthetic sapphire (Al_2O_3) reference at a heating rate of 10 °C/min in an open aluminum crucible in an argon flow.

To extrapolate the heat capacity data to the high-temperature region, the theoretical high-temperature limit was taken into account [54]: $C_p(T) = 3R + \alpha_V^2 \cdot VT/\beta_T$, where $\alpha_V = \frac{1}{V}\left(\frac{\delta V}{\delta T}\right)_P$ is the volumetric TEC, $\beta_T = \frac{-1}{V}\left(\frac{\delta V}{\delta P}\right)_T$ is the compressibility coefficient, V is the molar volume at absolute temperature T. For the approximation and extrapolation of C_p to the high-temperature range, we also used the following equation [55,56]:

$$C_p = a + bT + cT^2 + d/T^{0.5} + eT^2 \quad (1a)$$

Thermal conductivity κ of the bulk BYNO sample was calculated from the equation:

$$\kappa = \alpha \cdot \rho \cdot C_p, \quad (2a)$$

where κ, thermal diffusivity α, density ρ and C_p are expressed in W/m·K, m^2/s, kg/m^3, and J/kg·K, respectively.

3. Results and discussion

3.1. XRD, Raman spectrum, micromorphology and mechanical properties

The PXRD pattern of BYNO powder (Fig. 1) sintered at 1373−1773 K exhibited sharp, well-defined peaks, indicating high crystallinity and no

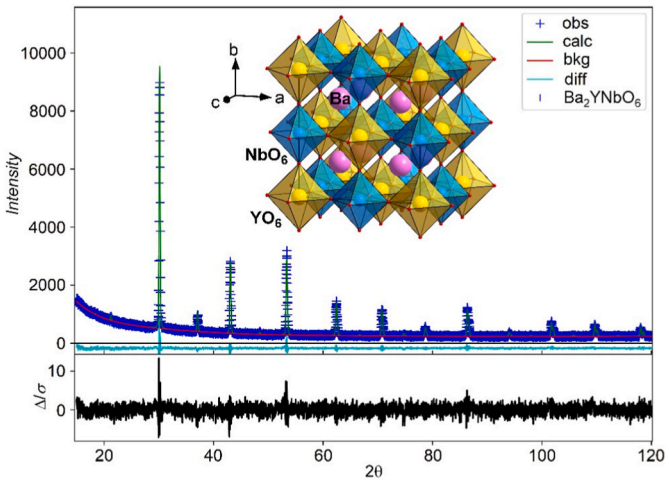

Fig. 1. PXRD pattern of the sintered sample and structure of Ba_2YNbO_6 (BYNO).

detectable secondary phases, which confirmed the successful synthesis of a single-phase Ba_2YNbO_6 (ICDD PDF-2 00-024-1042) with the double perovskite structure. The Rietveld refinement of the PXRD data, along with single-crystal X-ray diffraction analysis, confirmed that the crystal structure of BYNO is cubic. Detailed structural parameters derived from both single-crystal and Rietveld refinements are presented in Tables S1 and S2 (see Supporting Information). The values obtained are in good agreement with each other and with previously published data [57,58], validating the accuracy of our structural determinations. The single-crystal structure data (CIF) for Ba_2YNbO_6 were deposited at the CCDC with No. 2455110, https://www.ccdc.cam.ac.uk/structures/

The Raman spectrum of the BYNO powder (Fig. 2) further corroborated the formation of the desired structure, displaying characteristic vibrational modes consistent with the literature data for Ba_2YNbO_6 [15,59]. The spectrum contains the vibrational modes $T_{2g}(1)$, $T_{2g}(3)$ and A_{1g} characteristic of Ba_2YNbO_6. The observed peak at ~806 cm^{-1} (A_{1g}) is the result of symmetric stretching vibrations of the NbO_6 octahedron. The $T_{2g}(2)$ peak at 375 cm^{-1} corresponds to O−Nb−O bending vibrations, and the $T_{2g}(1)$ at 102 cm^{-1} is the result of the translational motion of Ba^{2+} cations [15,59].

The ceramic samples of BYNO obtained by the SPS method were high-density, nearly pore-free ceramic plates without visible pores and

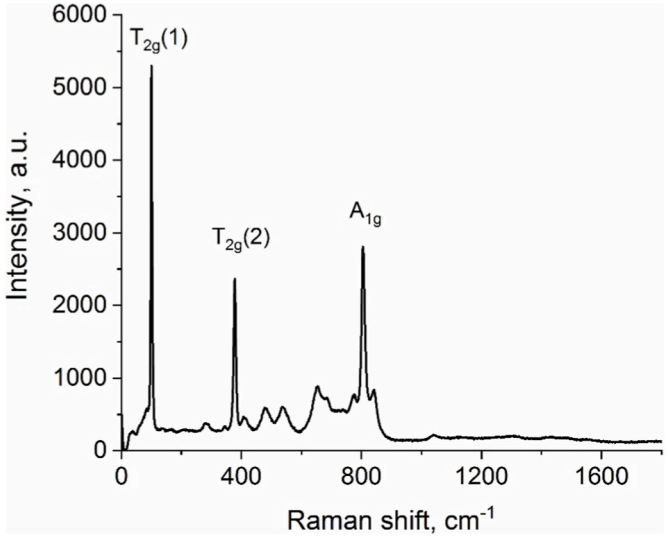

Fig. 2. Raman spectrum of sintered BYNO sample.

cracks (Fig. 3), with a relative density of 98–99% of the theoretical value. The geometric parameters of a typical sample are given in Table 1.

Fig. 4 shows the results of measuring the Young's modulus E and Vickers nanohardness HV of BYNO ceramic samples compacted by the SPS method. According to these data, BYNO ceramic in layers up to 50 nm thick has $E = 217 \pm 15$ GPa and average nanohardness HV = 7.18 ± 0.96 GPa. Our calculated values $E = 186$ GPa and $HV = 8.97$ GPa are in reasonable agreement with the experimental ones. Both of the mechanical characteristics measured for BYNO ceramic are comparable with those of YSZ coatings ($E = 210$ GPa and $HV = 13$–14 GPa) [2,4]. For comparison, a close structural analogue of BYNO, $BaZrO_3$ has E = 181–243 GPa and $HV = 4.95$–11.1 GPa [2,6,60].

As a result of our calculations using MTP potential for the tensor of elastic constants and elastic moduli of BYNO, we determined the bulk (B) and shear (G) moduli of BYNO are 136 GPa and 73 GPa, respectively. This yields to the Pugh's ratio of $G/B = 0.537$, which reflects the ductile–brittle distinction of the material and indicates the appropriate damage tolerance of BYNO ceramic for TBC applications. Comparing our findings in mechanical properties with another theoretical study [61] is shown in Table 5.

3.2. Thermophysical properties of BYNO

The melting point of BYNO has not been reported in the literature, so we attempted to determine it using a high-temperature microscope. However, the sample did not melt even at 2273 K, demonstrating remarkable thermal stability of BYNO.

The HT-PXRD study in the range of 0–1300 °C (Fig. S5) allowed us to determine the cubic unit cell parameter and TEC for BYNO as a function of temperature (Fig. 5). The data obtained revealed a monotonic increase in the lattice parameter from 8.4341(7) Å at room temperature to 8.5323(6) Å at 1300 °C (Fig. 5, *a*), indicating a positive TEC of BYNO. Our theoretical simulation (PIMD) predicts a lattice parameter of 8.44 Å at room temperature, which is in excellent agreement with our experimental results. P.W. Barnes et al. [62] also reported a measured lattice parameter of 8.44 Å, closely aligning with both our experimental and theoretical findings. In contrast, another theoretical study by A. Li et al., utilizing DFT, predicted a lattice parameter of 8.685 Å, which is higher than the experimental values [61]. We believe this discrepancy may be due to the use of the PBE functional in their calculations. The temperature dependence of the lattice parameter was accurately described by the following quadratic equation:

$$a(T) = 8.4322 + 6.440 \times 10^{-5}T + 8.989 \times 10^{-9}T^2 \ (T \text{ in } ^\circ C). \quad (3)$$

The TEC values calculated from the temperature dependence of the unit cell parameter can be described by the following linear function:

Table 1
Geometrical parameters and densities of BYNO samples sintered with SPS method.

h, mm	d, mm	m, g	ρ_{geom}, g/cm^3	ρ_{hydr}, g/cm^3
1.235	12.230	0.866	5.96909	6.08585

$$TEC(T) = 7.6445 \times 10^{-6} + 1.9692 \times 10^{-9}T \ (T \text{ in } ^\circ C). \quad (4)$$

The linear TEC of BYNO is (7.6–10.2) × 10^{-6} K^{-1} at 0–1300 °C (9.6 × 10^{-6} K^{-1} at 1000 °C), which agrees well with preliminary data (8.72 × 10^{-6} K^{-1}) [63], comparable with other perovskites (Table 2), higher than that for $La_2Zr_2O_7$ (9.1 × 10^{-6} K^{-1} at 30–1000 °C) [5], and lower than that for YSZ (about 10.7–11.5 × 10^{-6} K^{-1} at 30–1200 °C) [2,5]. Our analysis indicates that the Nb-O bond, as expected, is stronger than the Y-O and Ba-O bonds. The changes in the Y-O and Ba-O bonds with temperature are nearly twice as large as those of the Nb-O bond (Fig. S6), which determines their major contribution to the TEC of BYNO. The monotonic thermal expansion of BYNO, without any abrupt changes or phase transitions, indicates that the BYNO cubic structure is retained across the investigated temperature range.

Fig. 5 and Table 3 show a comparison of the calculated and experimental values for the temperature dependence of the lattice parameter and TEC for BYNO. It is noteworthy that both computational approaches correctly describe the functional dependence, and the differences between the calculated and experimental values are small.

Fig. 6 and Table 4 show the temperature dependence of the molar heat capacity of BYNO in the range of 0–1200 °C. The obtained values were used to calculate the thermal conductivity in the same temperature range.

The results of our thermal conductivity calculations are presented in Table 3 and Fig. 7. Fig. S3 and S4 display the running conductivity data, while Fig. 7 compares the thermal conductivity obtained from two calculation methods with experimental measurements as a function of temperature. Additionally, Fig. S7 contrasts the thermal conductivity calculated using classical HNEMD with that obtained from quantum-corrected HNEMD methods.

The thermal conductivity calculated at 1500 K (1227 °C), which closely corresponds to the operating conditions of TBC, is 1.35 W/(m·K) using the HNEMD method and 1.56 W/(m·K) using the BTE-EHM approach. In comparison, the experimental value is approximately 1.7 W/(m·K) (about 1.9 W/(m·K) at 1000 °C). As illustrated in Fig. 7, the value obtained from the BTE-EHM model aligns closely with our experimental measurements.

To further contextualize our findings, we compared our BTE results with a theoretical study by A. Li et al. [61], who employed the Clarke model [64] to estimate the minimum thermal conductivity of BYNO. A. Li et al. predicted thermal conductivity values of 2.5 W/(m·K) at 300 K

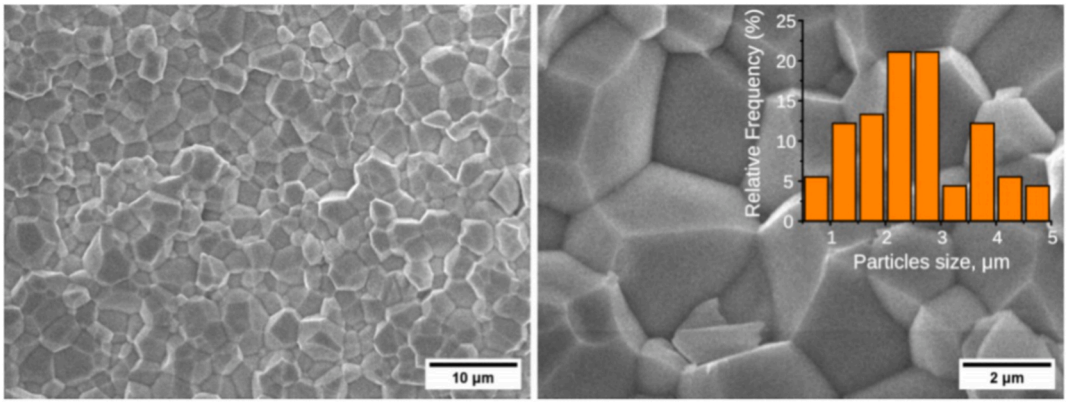

Fig. 3. Micrographs of a fractured BYNO sample. The insert shows the particle size distribution.

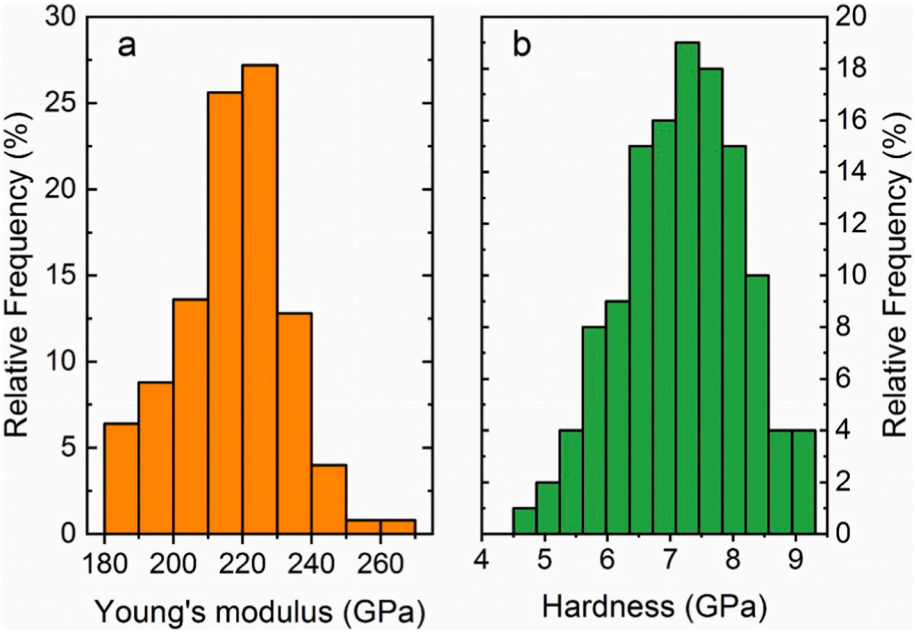

Fig. 4. Young's modulus and nanohardness (GPa) of bulk BYNO sample.

Table 2
Thermophysical and mechanical properties of BYNO compared with some perovskite-type TBC materials and YSZ [2,5].

Material	Melting point, °C	TEC, 10^{-6} K^{-1}	Thermal conductivity κ, W/(mK)	Young's modulus *E*, GPa	Hardness ^{HV}, GPa
Ba_2YNbO_6 (BYNO)	**> 2000**	**7.6–10.2 (0–1300 °C)**	**~1.9 (1000 °C)**	**217 ± 15**	**7.18 ± 0.96**
$BaZrO_3$	2690	7.9 (30–1000 °C)	3.42 (1000 °C)	181 ± 11	11.1 ± 1.9
$Ba(Mg_{1/3}Ta_{2/3})O_3$	3100	9.5–11.1 (200–1000 °C)	2.60 (1200 °C)	186 ± 2	12 ± 2
$SrZrO_3$	2650	8.75–10.9 (200–1000 °C)	2.08-2.30 (1200 °C)	170 ± 4	13 ± 1
$Sr(Zr_{0.9}Gd_{0.1})O_{2.95}$	—	9.2–10.6 (200–1000 °C)	1.85 (1200 °C)	150 ± 5	9.2 ± 0.9
YSZ	2680	10.7–11.5 (30–1000 °C)	2.12–2.20 (1000 °C)	210 ± 10	13 ± 1

Table 3
Calculated TEC (PIMD) and thermal conductivity of BYNO at different temperatures.

Linear TEC[a], × 10^{-6} K^{-1}		Thermal conductivity κ, W/(m·K)					
		HNEMD			BTE (EHM)		
1000 K	1500 K	300 K	1000 K	1500 K	300 K	1000 K	1500 K
9.47	10.54	3.83 ± 0.15	1.73 ± 0.08	1.35 ± 0.07	4.03	1.95	1.56

[a] Measured TEC values are 9.08 × 10^{-6} K^{-1} at 1000 K and 10.06 × 10^{-6} K^{-1} at 1500 K.

Table 4
Molar heat capacity C_p, J/(mol·K) of Ba_2YNbO_6 (M = 552.46 g/mol) at different temperatures.

300 K	500 K	700 K	900 K	1100 K	1300 K	1500 K
204.9 ± 4.1	228.4 ± 4.6	238.3 ± 4.8	243.9 ± 4.9	247.3 ± 4.9	248.5 ± 5.0	250.5 ± 5.0

Table 5
Structural parameters *a* (Å), elastic modulus *B*, *G* and *E* (GPa), Hardness *Hv* (GPa), and Pugh's ratio.

Compound	Experiment		Theory	
	This work	Ref [62]	This work	Ref [61]
a (T = 27 °C)	8.43	8.44	8.45	8.68 (T = −273 °C)
B			136	138
G			73	80
E	217		186	202
Hv	7.18		8.97	
G/B			0.537	0.58

and 1.3 W/(m·K) at 500 K, both of which are lower than our BTE results (see Table 3). The reason for this discrepancy lies in the simplicity of the Clarke model, which cannot fully account for the anharmonicity of the system at high temperatures. Like other conventional BTE models, it tends to underestimate thermal conductivity for highly anharmonic materials, an issue we addressed in our previous study [38].

Our measured thermal conductivity for BYNO is significantly lower than that of most perovskites studied (as shown in Table 2) and is even slightly lower than that of YSZ (approximately 2 W/(m·K) at 1000 °C) [1,2].

It is worth noting that, due to MD simulations using an 8 × 8 × 8 supercell and a cooling rate of 625 K/ns, we observed a phase transition

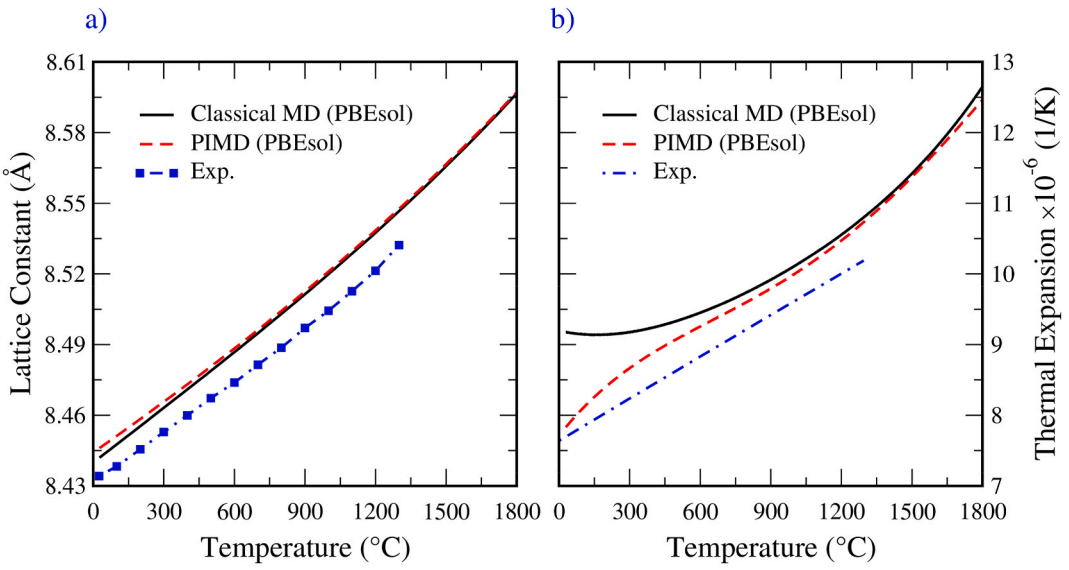

Fig. 5. a) Lattice constant of BYNO as a function of temperature. (b) Thermal expansion coefficient as a function of temperature.

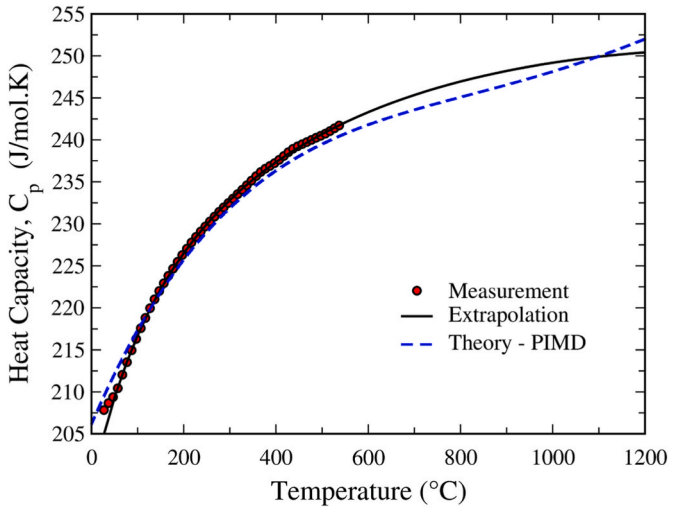

Fig. 6. Molar heat capacity of bulk BYNO ceramic in the range of 0−1200 °C.

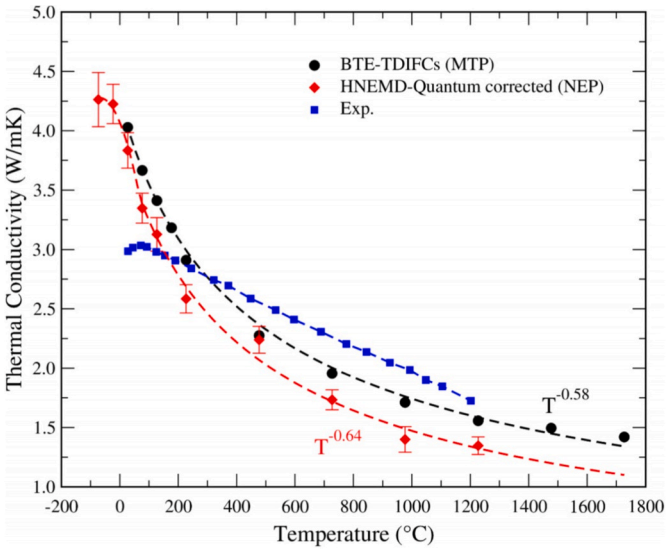

Fig. 7. Comparison of experimental and theoretical thermal conductivity of BYNO, as determined by the BTE-EHM and HNEMD methods.

from the tetragonal to the cubic phase at −20°C for classical MD and −53°C for PIMD (see Fig. S8). Indeed, DSC experiments revealed a thermal anomaly within the range from −23 to 7°C, characterized by a distinct peak at −10.6 ± 2.0°C (refer to Fig. S9). The presence of this anomaly is indicative of a structural rearrangement within BYNO lattice, corresponding to a displacive phase transition.

These results are in good agreement with the experimental data on the second-order phase transition $Fm\bar{3}m \rightarrow I4/m$ in BYNO at −13°C [65]. However, our low-temperature PXRD data showed no deviations from the linear dependence of TEC for BYNO at these temperatures. This observation can be explained by the minor changes in the structure and unit cell volume of BYNO during this transition.

4. Conclusions

Based on a combination of detailed simulations of thermal conductivity, thermal expansion, and mechanical properties with experimental measurements, we studied double perovskite Ba_2YNbO_6 (BYNO) to evaluate its applicability as a potential material for TBCs. The bulk BYNO ceramics, prepared by spark plasma sintering (SPS) at 1700 °C, was investigated in terms of its microstructure, thermal, and mechanical properties. BYNO has higher thermal stability (a high melting point and no phase transitions up to 2000 °C) and lower thermal conductivity (~1.9 W/(m·K) at 1000 °C) compared with YSZ (~2.1 W/(m·K) at 1000 °C) [2,5]. At the same time, we confirmed a minor structural rearrangement (second-order phase transition) near −10 °C. The TEC of BYNO is moderate (about 9.6 × 10^{-6} K^{-1} at 1000 °C), and close to $La_2Zr_2O_7$ and the perovskite-type TBC materials, but lower than for YSZ (Table 2). The mechanical properties of BYNO (Young's modulus 217 ± 15 GPa, Vickers hardness 7.18 ± 0.96 GPa) are comparable to those of YSZ. According to our MTP calculations, the bulk and shear moduli of BYNO are 136 GPa and 73 GPa, respectively, resulting in a Pugh's ratio G/B = 0.537, which is also a favorable value for TBC materials. Our results strongly suggest BYNO as a potential thermal barrier coating material, provided it will display good adhesion and high chemical stability in real operating conditions. Furthermore, the functional properties of BYNO could be improved by cation doping, forming solid solutions with other perovskites, increasing the porosity of BYNO coatings, or using advanced deposition techniques for microstructure

modification.

CRediT authorship contribution statement

S.F. Solodovnikov: Writing – review & editing, Writing – original draft, Validation, Supervision, Project administration, Data curation, Conceptualization. **M. Zeraati:** Writing – review & editing, Visualization, Validation, Software, Formal analysis. **A.B. Kuznetsov:** Writing – review & editing, Visualization, Investigation, Formal analysis. **E.S. Zolotova:** Investigation. **A.R. Nasyrbaev:** Writing – review & editing, Investigation. **I.P. Gulyaev:** Writing – review & editing, Investigation. **I. K. Igumenov:** Writing – review & editing, Supervision. **R.A. Shutilov:** Writing – review & editing, Visualization, Investigation. **E.A. Maksimovsky:** Investigation. **D.P. Pishchur:** Writing – review & editing, Visualization, Investigation. **V.N. Yudin:** Investigation. **V.V. Lukashov:** Visualization, Validation. **I.V. Korolkov:** Visualization, Investigation. **A.P. Maltsev:** Writing – review & editing, Investigation. **A.R. Oganov:** Writing – review & editing, Validation, Supervision, Methodology.

Declaration of competing interest

The authors declare that they have no known competing financial interests or personal relationships that could have appeared to influence the work reported in this paper.

Acknowledgements

This work was supported by the Russian Science Foundation, grant No. 23-13-00117 (https://rscf.ru/project/23-13-00117/). A.R.O.'s research was conducted with the support of the NTI Fund under grant agreement No. 70-2025-000715 dated May 21, 2025. Calculations were performed on Oleg and Zhores supercomputers of Skoltech. The powder and single-crystal XRD data were obtained using the facilities of Shared Equipment Center of Nikolaev Institute of Inorganic Chemistry SB RAS. Analytical measurements were performed at Shared Research Facilities for Multi-elemental and Isotope Research of Sobolev Institute of Geology and Mineralogy SB RAS. The authors are grateful to Dr. R.E. Nikolaev for measurements of a powder BYNO sample on a high-temperature microscope.

Appendix A. Supplementary data

Supplementary data to this article can be found online at https://doi.org/10.1016/j.ceramint.2026.02.315.

Appendix A

All DFT calculations were performed using PBEsol [66] functional with plane-wave basis set with 520 eV energy cutoff, and PAW [67] method, implemented in the VASP code [68]. To constract training set we used a supercell consisting of 40 atoms and we used 2 × 2 × 2 Γ-centered Monkhorst-Pack mesh of k points Integration over the Brillouin zone.

For performing simulations first we trained 18th level MTP-type [43] MLIP using active learning approach [69] and MLIP-2 package [70]. The final training set consists of 1177 configurations; root mean square errors (RMSE) for energy per atom and forces are 2.1 meV and 78.8 meV/Å compared to the DFT data. MTP potential was used for elastic constants calculations.

For the HNEMD and TEC calculations we used neuroevolution potential (NEP) [71], which was trained using the same dataset, as the MTP; RMSE for energy per atom and forces in case of NEP are 1.7 meV and 74.0 meV/Å. The parameter $\boldsymbol{F}_e$ in formula (1) has the dimension of inverse length and is chosen sufficiently small (in this work it was set to 5×10^{-5} Å^{-1}), to ensure the system remains in the linear response regime. To perform MD simulation we constructed 8 × 8 × 8 supercell contain 20480 atoms.

For constructing temperature-dependent interatomic force constants (TDIFCs), we performed MD simulations in the canonical ensemble for each temperature in a supercell for 250 ps (each equilibrium lattice constant was calculated using the MD simulation in the NPT ensemble for 60 ps) and chose 400 configurations which each of them contains 320 atoms.

To construct second and third order interatomic force constants (IFCs) we used 4 × 4 × 4 supercell of primitive cell. After testing convergence of thermal conductivity value at room temperature we chose dense 10 × 10 × 10 grid of q points in Brillouin zone for the self-consistent solutions of BTE.

References

[1] S. Ghosh, Thermal barrier ceramic coatings — a review, in: A.M.A. Mohamed (Ed.), Advanced Ceramic Processing, IntechOpen, Rijeka, 2015, pp. 111–138. https://www.intechopen.com/chapters/49216.

[2] L.L. Huang, H.M. Meng, J. Tang, S. Li, Z.Q. Yu, Overview on double ceramic layer thermal barrier coatings, Adv. Mat. Res. 1053 (2014) 364–372. https://dx.doi.org/10.4028/www.scientific.net/AMR.1053.364.

[3] K. Mondal, L. Nuñez, C.M. Downey, I.J. van Rooyen, Thermal barrier coatings overview: design, manufacturing, and applications in high-temperature industries, Ind. Eng. Chem. Res. 60 (2021) 6061–6077, https://doi.org/10.1021/acs.iecr.1c00788.

[4] S.M. Lakiza, M.I. Grechanyuk, O.K. Ruban, V.P. Redko, M.S. Glabay, O. B. Myloserdov, O.V. Dudnik, S.V. Prokhorenko, Thermal barrier coatings: current status, search, and analysis, Powder Metall. Met. Ceram. 57 (2018) 82–113, https://doi.org/10.1007/s11106-018-9958-0.

[5] J. Song, L. Wang, J. Yao, H. Dong, Multi-scale structural design and advanced materials for thermal barrier coatings with high thermal insulation: a review, Coatings 13 (2023) 343, https://doi.org/10.3390/coatings13020343.

[6] R. Vaßen, X. Cao, F. Tietz, D. Basu, D. Stöver, Zirconates as new materials for thermal barrier coatings, J. Am. Ceram. Soc. 83 (2000) 2023–2028, https://doi.org/10.1111/j.1151-2916.2000.tb01506.x.

[7] W. Ma, M.O. Jarligo, D.E. Mack, D. Pitzer, J. Malzbender, R. Vaßen, D. Stöver, New generation perovskite thermal barrier coating materials, J. Thermal Spray Technol. 17 (2008) 831–837, https://doi.org/10.1007/s11666-008-9239-4.

[8] W. Ma, P. Li, H. Dong, Y. Bai, J. Zhao, X. Fan, Y_2O_3 and Yb_2O_3 co-doped strontium hafnate as a new thermal barrier coating material, J. Thermal Spray Technol. 23 (2014) 154–159, https://doi.org/10.1007/s11666-013-0006-9.

[9] J. Yuan, J. Sun, J. Wang, H. Zhang, S. Dong, J. Jiang, L. Deng, X. Zhou, X. Cao, $SrCeO_3$ as a novel thermal barrier coating candidate for high-temperature applications, J. Alloys Compd. 740 (2018) 519–528, https://doi.org/10.1007/s11666-013-0006-9.

[10] Y. Cao, Q. Wang, X. Ning, Y. Liu, Evaluation of the phase stability, and mechanical and thermal properties of $Ba(Sr_{1/3}Ta_{2/3})O_3$ as a potential ceramic material for thermal barrier coatings, Ceram. Int. 45 (2019) 12989–12993, https://doi.org/10.1016/j.ceramint.2019.03.227.

[11] T. Ogawa, T. Matsudaira, D. Yokoe, E. Kawai, N. Kawashima, C.A.J. Fisher, Y. Habu, T. Kato, S. Kitaoka, Spontaneously formed nanostructures in double perovskite rare-earth tantalates for thermal barrier coatings, Acta Mater. 216 (2021) 117152, https://doi.org/10.1016/j.actamat.2021.117152.

[12] M.O. Jarligo, D.E. Mack, R. Vassen, D. Stöver, Application of plasma-sprayed complex perovskites as thermal barrier coatings, J. Thermal Spray Technol. 18 (2009) 187–193, https://doi.org/10.1007/s11666-009-9302-9.

[13] S. Vasala, M. Karppinen, $A_2B'B''O_6$ perovskites: a review, Progr, Solid State Chem. 43 (2015) 1–36, https://doi.org/10.1016/j.progsolidstchem.2014.08.001.

[14] W.L. Zhou, Q.L. Zhang, J.Y. Gao, W.P. Liu, L.H. Ding, S.T. Yin, Structures and luminescence properties of Yb^{3+} in the double perovskites $Ba_2YB'O_6$ ($B' = Ta^{5+}$, Nb^{5+}) phosphors, Chin. Phys. B 20 (2011) 016101, https://doi.org/10.1088/1674-1056/20/1/016101.

[15] A. Fu, Q. Pang, H. Yang, L. Zhou, Ba_2YNbO_6:Mn^{4+}-based red phosphor for warm white light-emitting diodes (WLEDs): photoluminescent and thermal characteristics, Opt. Mater. 70 (2017) 144–152, https://doi.org/10.1016/j.optmat.2017.05.028.

[16] K.V. Paulose, J. Koshy, A.D. Damodaran, YBa_2NbO_6: synthesis, properties and compatibility with $YBa_2Cu_3O_{7-\delta}$, Physica C 193 (1992) 273–276, https://doi.org/10.1016/0921-4534(92)90728-U.

[17] S.H. Wee, C. Cantoni, A. Goyal, Epitaxial growth of Ba_2YNbO_6 films on biaxially-textured NiW substrates as a multifunctional single buffer layer for high J_c epitaxial YBCO film, MRS Commun. 5 (2015) 533–538, https://doi.org/10.1557/mrc.2015.62.

[18] Y. Xu, H.L. Suo, J.-C. Grivel, M. Liu, X. Zhang, Y. Zhou, J. Liu, Z. Zhang, Synergistic effects on the nanostrain in YBCO films double-doped with positive mismatch perovskite (Ba_2YNbO_6) and negative mismatch perovskite ($LaAlO_3$), Cryst. Growth Des. 20 (2020) 3449–3455, https://doi.org/10.1021/acs.cgd.0c00227.

[19] K. Prasad, S. Bhagat, Priyanka, K. AmarNath, K.P. Chandra, A.R. Kulkarni, Electrical properties of $BaY_{0.5}Nb_{0.5}O_3$ ceramic: impedance spectroscopy analysis, Physica B 405 (2010) 3564–3571, https://doi.org/10.1016/j.physb.2010.05.041.

[20] D.J. Evans, Homogeneous NEMD algorithm for thermal conductivity—Application of non-canonical linear response theory, Phys. Lett. 91 (1982) 457–460, https://doi.org/10.1016/0375-9601(82)90748-4.

[21] Z. Fan, H. Dong, A. Haju, T. Ala-Nissila, Homogeneous nonequilibrium molecular dynamics method for heat transport and spectral decomposition with many-body potentials, Phys. Rev. B 99 (2019) 064308, https://doi.org/10.1103/PhysRevB.99.064308.

[22] Z. Fan, Y. Wang, P. Ying, K. Song, J. Wang, Y. Wang, Z. Zeng, K. Xu, E. Lindgren, J. M. Rahm, A.J. Gabourie, J. Liu, H. Dong, J. Wu, Y. Chen, Z. Zhong, J. Sun, P. Erhart, Y. Su, T. Ala-Nissila, GPUMD: a package for constructing accurate machine-learned potentials and performing highly efficient atomistic simulations, J. Chem. Phys. 157 (2022) 114801, https://doi.org/10.1063/5.0106617.

[23] Z. Fan, W. Chen, V. Vierimaa, A. Harju, Efficient molecular dynamics simulations with many-body potentials on graphics processing units, Comput. Phys. Commun. 218 (2017) 10–16, https://doi.org/10.1016/j.cpc.2017.05.003.

[24] D.J. Evans, B.L. Holian, The Nose–Hoover thermostat, J. Chem. Phys. 83 (1985) 4069–4074, https://doi.org/10.1063/1.449071.

[25] R.E. Peierls, On the kinetic theory of thermal conduction in crystals, Ann. Phys. 395 (1929) 1055–1100, https://doi.org/10.1142/9789812795779_0004.

[26] M. Omini, A. Sparavigna, An iterative approach to the phonon Boltzmann equation in the theory of thermal conductivity, Physica B: Condens. Matter. 212 (1995) 101–112, https://doi.org/10.1016/0921-4526(95)00016-3.

[27] M. Omini, A. Sparavigna, Beyond the isotropic model approximation in the theory of thermal conductivity, Phys. Rev. B 53 (1996) 9064–9073, https://doi.org/10.1103/PhysRevB.53.9064.

[28] P. Souvatzis, O. Eriksson, M.I. Katsnelson, S.P. Rudin, Entropy driven stabilization of energetically unstable crystal structures explained from first principles theory, Phys. Rev. Lett. 100 (2008) 095901, https://doi.org/10.1103/PhysRevLett.100.095901.

[29] O. Hellman, I.A. Abrikosov, S.I. Simak, Lattice dynamics of anharmonic solids from first principles, Phys. Rev. B 84 (2011) 180301, https://doi.org/10.1103/PhysRevB.84.180301.

[30] F. Eriksson, E. Fransson, P. Erhart, The hiphive package for the extraction of high-order force constants by machine learning, Adv. Theory Simul. 2 (2019) 1800184, https://doi.org/10.1002/adts.201800184.

[31] W. Li, J. Carrete, N. Katcho, N. Mingo, ShengBTE: a solver of the Boltzmann transport equation for phonons, Computer Phys. Comm. 185 (2014) 1747–1758, https://doi.org/10.1016/j.cpc.2014.02.015.

[32] A.J. Gabourie, Z. Fan, T. Ala-Nissila, E. Pop, Spectral decomposition of thermal conductivity: comparing velocity decomposition methods in homogeneous molecular dynamics simulations, Phys. Rev. B 103 (2021) 205421, https://doi.org/10.1103/PhysRevB.103.205421.

[33] G.J. Martyna, M.L. Klein, M. Tuckerman, Nosé–Hoover chains: the canonical ensemble via continuous dynamics, J. Chem. Phys. 97 (1992) 2635–2643, https://doi.org/10.1063/1.463940.

[34] R.P. Feynman, A.R. Hibbs, The Path Integral Formulation of Quantum Mechanics, McGraw-Hill, New York, 1965.

[35] M. Parrinello, A. Rahman, Study of an F center in molten KCl, J. Chem. Phys. 80 (1984) 860, https://doi.org/10.1063/1.446740.

[36] P. Ying, W. Zhou, L. Svensson, E. Berger, E. Fransson, F. Eriksson, K. Xu, T. Liang, J. Xu, B. Song, S. Chen, P. Erhart, Z. Fan, Highly efficient path-integral molecular dynamics simulations with GPUMD using neuroevolution potentials: case studies on thermal properties of materials, J. Chem. Phys. 162 (2025) 064109, https://doi.org/10.1063/5.0241006.

[37] M. Ceriotti, M. Parrinello, T.E. Markland, D.E. Manolopoulos, J. Chem. Phys. 133 (2010) 124104, https://doi.org/10.1063/1.3489925.

[38] M. Zeraati, A.R. Oganov, T. Fan, S.F. Solodovnikov, Searching for low thermal conductivity materials for thermal barrier coatings: a theoretical approach, Phys. Rev. Mater. 8 (2024) 033601, https://doi.org/10.1103/PhysRevMaterials.8.033601.

[39] M. Zeraati, A.R. Oganov, A.P. Maltsev, S.F. Solodovnikov, Computational screening of complex oxides for next-generation thermal barrier coatings, J. Appl. Phys. 137 (2025) 065106, https://doi.org/10.1063/5.0253010.

[40] W. Voigt, Lehrbuch Der Kristallphysik (Mit Ausschluss Der Kristalloptik) (B.G, Teubner, Leipzig, Berlin, 1910.

[41] A. Reuss, Berechnung der Fließgrenze vonMischkristallen auf Grund der Plastizitätsbedingung für Einkristalle, Z. Angew. Math. Mech. 9 (1929) 49, https://doi.org/10.1002/zamm.19290090104.

[42] R. Hill, The elastic behaviour of a crystalline aggregate, Proc. Phys. Soc. 65 (1952) 349, https://doi.org/10.1088/0370-1298/65/5/307.

[43] A.V. Shapeev, Moment tensor potentials: a class of systematically improvable interatomic potentials, Multiscale Model. Simul. 14 (2016) 1153–1173, https://doi.org/10.1137/15M1054183.

[44] X. Chen, H. Niu, D. Li, Y. Li, Modeling hardness of polycrystalline materials and bulk metallic glasses, Intermetallics 19 (2011) 1275–1281, https://doi.org/10.1016/j.intermet.2011.03.026.

[45] H.M. Rietveld, A profile refinement method for nuclear and magnetic structures, J. Appl. Cryst. 2 (1969) 65–71, https://doi.org/10.1107/S0021889869006558.

[46] B.H. Toby, R.B. Von Dreele, GSAS-II: the genesis of a modern open-source all purpose crystallography software package, J. Appl. Cryst. 46 (2013) 544–549, https://doi.org/10.1107/S0021889813003531.

[47] A. Le Bail, H. Duroy, J.L. Fourquet, Ab-initio structure determination of $LiSbWO_6$ by X-ray powder diffraction, Mater. Res. Bull. 23 (1988) 447, https://doi.org/10.1016/0025-5408(88)90019-0.

[48] Bruker. APEX3 Version 2016.5-0, Bruker AXS, Inc, Madison, Wisconsin, USA, 2016.

[49] G.M. Sheldrick, SHELXT - integrated space-group and crystal-structure determination, Acta Cryst. A 71 (2015) 3–8, https://doi.org/10.1107/S2053273314026370.

[50] G.M. Sheldrick, Crystal structure refinement with SHELXL, Acta Cryst. C 71 (2015) 3–8, https://doi.org/10.1107/S2053229614024218.

[51] O.V. Dolomanov, L.J. Bourhis, R.J. Gildea, J.A.K. Howard, H. Puschmann, OLEX2: a complete structure solution, refinement and analysis program, J. Appl. Cryst. 42 (2009) 339–341, https://doi.org/10.1107/S0021889808042726.

[52] YaI. Gibner, I.G. Vasilyeva, Rapid heating in high-temperature thermomicroscopic analysis, J. Therm. Anal. 53 (1998) 151–160, https://doi.org/10.1023/A:1010115620439.

[53] W.C. Oliver, G.M. Pharr, An improved technique for determining hardness and elastic modulus using load and displacement sensing indentation experiments, J. Mater. Res. 7 (1992) 1564–1583, https://doi.org/10.1557/JMR.1992.1564.

[54] R.G. Berman, T.H. Brown, Heat capacity of minerals in the system Na_2O-K_2O-CaO-MgO-FeO-F_2O_3-$A1_2O_3$-SIO_2-TiO_2- H_2O- CO_2: representation, estimation, and high temperature extrapolation, Contr. Mineral. and Petrol. 94 (1986) 168–183, https://doi.org/10.1007/BF00592944.

[55] D. de Ligny, P. Richet, High-temperature heat capacity and thermal expansion of $SrTiO_3$ and $SrZrO_3$ perovskites, Phys. Rev. B 53 (1996) 3013–3022, https://doi.org/10.1103/PhysRevB.53.3013.

[56] G.M. Anderson, Thermodynamics of Natural Systems, second ed., Cambridge University Press, 2005.

[57] P.W. Barnes, M.W. Lufaso, P.M. Woodward, Structure determination of $A_2M^{3+}TaO_6$ and $A_2M^{3+}NbO_6$ ordered perovskites: octahedral tilting and pseudosymmetry, Acta Cryst B62 (2006) 384–396, https://doi.org/10.1107/S0108768106002448.

[58] W.T. Fu, D.J.W. Ijdo, New insight into the symmetry and the structure of the double perovskites Ba_2LnNbO_6 (*Ln* = lanthanides and Y), J. Solid State Chem. 179 (2006) 1022–1028, https://doi.org/10.1016/j.jssc.2005.12.031.

[59] W. Li, L. Ning, P.A. Tanner, Double perovskite structure: a vibrational and luminescence investigation providing a perspective on crystal field strength, J. Phys. Chem. A 116 (2012) 7337–7344, https://doi.org/10.1021/jp303626v.

[60] S. Yamanaka, M. Fujikane, T. Hamaguchi, H. Muta, T. Oyama, T. Matsuda, S. Kobayashi, K. Kurosaki, Thermophysical properties of $BaZrO_3$ and $BaCeO_3$, J. Alloys Compd. 359 (2003) 109–113, https://doi.org/10.1016/S0925-8388(03)00214-7.

[61] X. Li, X. Zhang, F. Wang, B. Liu, Ba_2MNO_6 (M = Y, Sc; N = Nb, V, Ta) as next-generation double perovskite oxides: a comprehensive first principles study on the stability, mechanical properties, electronic properties and thermophysical properties, Physica Scripta 100 (2025) 085926, https://doi.org/10.1088/1402-4896/adf0a6.

[62] P.W. Barnes, M.W. Lufaso, P.M. Woodward, Structure determination of $A_2M^{3+}TaO_6$ and $A_2M^{3+}NbO_6$ ordered perovskites: octahedral tilting and pseudosymmetry, Acta Crystallogr. Sect. B Struct. Sci. 62 (2006) 384–396, https://doi.org/10.1107/S0108768106002448.

[63] A. Iakovleva, Study of Novel Proton Conductors for High Temperature Solid Oxide Cells, Phd Thesis, Université Paris-Saclay, Paris, 2015. https://theses.hal.science/tel-01294613v1/file/IAKOVLEVA_2015_diffusion.pdf.

[64] D.R. Clarke, Materials selection guidelines for low thermal conductivity thermal barrier coatings, Surf. Coat. Technol. 67 (2003) 163–164, https://doi.org/10.1016/S0257-8972(02)00593-5.

[65] I. Gregora, J. Petzelt, J. Pokorný, V. Vorlíček, Z. Zikmund, R. Zurmühlen, N. Setter, Raman spectroscopy of the zone centre improper ferroelastic transition in ordered $Ba(Y_{1/2}Ta_{1/2})O_3$ complex perovskite ceramic, Solid State Commun. 94 (1995) 899–903, https://doi.org/10.1016/0038-1098(95)00192-1.

[66] J.P. Perdew, A. Ruzsinszky, G.I. Csonka, O.A. Vydrov, G.E. Scuseria, L. A. Constantin, X. Zhou, K. Burke, Restoring the density-gradient expansion for exchange in solids and surfaces, Phys. Rev. Lett. 100 (2008) 136406, https://doi.org/10.1103/PhysRevLett.100.136406.

[67] P.E. Blöchl, Projector augmented-wave method, Phys. Rev. B 50 (1994) 17953, https://doi.org/10.1103/PhysRevB.50.17953.

[68] G. Kresse, J. Furthmüller, Efficient iterative schemes for *ab initio* total-energy calculations using a plane-wave basis set, Phys. Rev. B 54 (1996) 11169, https://doi.org/10.1103/PhysRevB.54.11169.

[69] E.V. Podryabinkin, A.V. Shapeev, Active learning of linearly parametrized interatomic potentials, Comput. Mater. Sci. 140 (2017) 171–180, https://doi.org/10.1016/j.commatsci.2017.08.031.

[70] I.S. Novikov, K. Gubaev, E.V. Podryabinkin, A.V. Shapeev, The MLIP package: moment tensor potentials with MPI and active learning, Mach. Learn.: Sci. Technol. 2 (2020) 025002, https://doi.org/10.1088/2632-2153/abc9fe.

[71] Z. Fan, Z. Zeng, C. Zhang, Y. Wang, K. Song, H. Dong, Y. Chen, T. Ala-Nissila, Neuroevolution machine learning potentials: combining high accuracy and low cost in atomistic simulations and application to heat transport, Phys. Rev. B 104 (2021) 104309, https://doi.org/10.1103/PhysRevB.104.104309.